



Regular paper



# High-efficiency CMOS rectifiers with wide power dynamic range based on leakage-current-suppressing and adaptive-biasing techniques for RF energy harvesting

Di Luo <sup>a</sup>, Jian Liu <sup>a</sup>,\*, Kang Zeng <sup>a</sup>, Rui Wang <sup>a</sup>, Meijing Wang <sup>b</sup><sup>a</sup> School of Integrated Circuits, Guangdong University of Technology, Guangzhou, 510006, Guangdong Province, China<sup>b</sup> School of Biomedical and Pharmaceutical Sciences, Guangdong University of Technology, Guangzhou, 510006, Guangdong Province, China

## ARTICLE INFO

## Keywords:

CMOS rectifier  
High power conversion efficiency  
Leakage-current-suppressing (LCS)  
RFEH  
Wide power dynamic range  
Wireless power transfer (WPT)

## ABSTRACT

This article proposes two high-efficiency CMOS rectifiers with wide power dynamic range (WPDR) for radio frequency energy harvesting (RFEH). The first rectifier (LCS-R1) incorporates a leakage-current-suppression (LCS) technique to enhance power conversion efficiency (PCE) by dynamically reducing the drain-source voltage ( $V_{DS}$ ) of the main transmission MOSFETs, which minimizes power dissipation. Based on the LCS-R1 architecture, the second rectifier (LCSAB-R2) integrates gate and substrate adaptive-biasing techniques to reduce the effective threshold voltage ( $V_{TH}$ ) of the MOSFETs. The LCS and adaptive-biasing techniques demonstrate good compatibility, enabling the LCSAB-R2 achieves improved PCE and extended power dynamic range (PDR). To validate the proposed schemes, both rectifiers are implemented in a TSMC 40 nm CMOS process with chip areas of 0.0121 mm<sup>2</sup> and 0.0036 mm<sup>2</sup>, respectively. Simulation results demonstrate that LCS-R1 and LCSAB-R2 achieve peak PCEs of 69% and 89.4% at 433 MHz with a 200 kΩ load. Furthermore, the PDR for PCE > 40% are 23 dB and 27.7 dB, respectively.

## 1. Introduction

Wireless energy harvesting is a technology that utilizes RF signals in the environment as an energy source, which has broad application prospects and potential. With the popularization of low-power electronic devices and the rapid development of wireless sensor networks [1,2], it has become increasingly important to find sustainable energy solutions to replace traditional battery power [3]. RF energy harvesting has garnered widespread attention as a sustainable and efficient energy solution.

RFEH technology is widely utilized in wireless power supply applications, including wireless sensor networks (WSNs) and wireless power transmission (WPT). Its adoption aims to decrease battery usage, reduce environmental pollution, and improve system durability. WSNs are networks of many distributed sensor nodes for collecting and transmitting environmental data [4]. These sensor nodes are typically powered by batteries, which have limited capacity. As a result, their batteries require periodic replacement and disposal, which can pose environmental pollution risks if not handled properly. RFEH technology offers an alternative power supply solution for WSNs, reducing the reliance on batteries in such devices.

By integrating RFEH technology into WSNs, sensor nodes can harvest energy from the surrounding RF environment, which typically provides power densities ranging from 0.08 nW/cm<sup>2</sup> – 1 μW/cm<sup>2</sup> [5]. This approach not only eliminates the need for frequent battery replacements, reducing the generation of used batteries and their associated environmental pollution, but also significantly lowers the maintenance costs of WSNs by saving time and human resources.

The application of RFEH technology has the potential to greatly enhance the sustainability and reliability of WSNs [6]. By embedding RFEH systems into individual wireless communication devices, the reliance on traditional batteries can be substantially minimized. This integration reduces the size of the required batteries, decreases the frequency of replacements, and, in some cases, may eliminate the need for batteries altogether.

RFEH technology faces several challenges in wireless power supply applications, including the low energy density of RF signals, limited transmission distance, low energy conversion efficiency. Additionally, fluctuations in signal strength and availability can adversely affect the performance and stability of RF energy harvesting systems [7]. To address these challenges, achieving high PCE and a WPDR is critical in the design of RF energy harvesting systems. Moreover, evaluating

\* Corresponding author.

E-mail address: [xzliujian@gdut.edu.cn](mailto:xzliujian@gdut.edu.cn) (J. Liu).

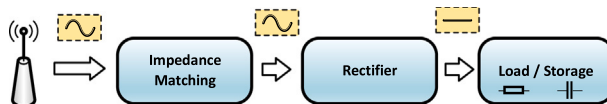


**Fig. 1.** Conceptual block diagram of RF energy harvesting system.

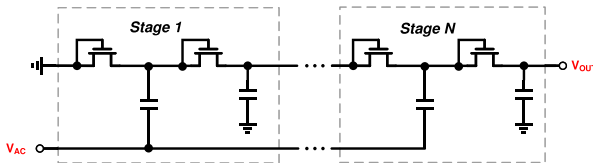


**Fig. 2.** Schematic of the N-stage Dickson charge pump rectifier.

the specific application scenarios is essential to ensure the system's feasibility and adaptability. This evaluation helps guarantee that the RF energy harvesting system meets the power supply requirements of the intended application while maintaining reliable operation.

A conceptual block diagram of the RF energy harvesting system is shown in Fig. 1. The system includes an antenna or receiver that collects RF energy and channels it through a matching network to an RF-to-DC rectifier, which efficiently converts the harvested RF signals into DC power [8]. The converted DC energy is then delivered to a power management circuit for voltage regulation and current control, ensuring the device's operational requirements are met. Additionally, some RF energy harvesting systems integrate energy storage devices, such as batteries or supercapacitors, to store energy and provide power when RF signals are unavailable. Power losses occur during the transmission of RF energy from the antenna input to the load, with the RF-DC converter or rectifier module being the primary source of these losses. Therefore, minimizing energy loss in this module is a key focus of research.

Fig. 2 shows a traditional Dickson rectifier design that uses a diode-connected MOSFET instead of a Schottky diode. This approach was more cost-effective due to its compatibility with CMOS processes. However, the diode-connected MOSFETs had a high threshold voltage, which reduced both PCE and sensitivity at low input power levels. To address this issue, a static threshold compensation technique was introduced. While this technique successfully lowered the threshold voltage, it also increased power loss due to reverse leakage current. Subsequently, differential-driven CMOS rectifiers were proposed [9], as illustrated in Fig. 3. This topology reduces on-resistance and reverse leakage current in MOSFETs, enhancing sensitivity with its differential input design. Nevertheless, at high input power levels, the reverse leakage current increases significantly, leading to a drop in PCE and limiting the dynamic range (DR) of the CCDD topology. Various methods and techniques have since been developed to mitigate reverse leakage current. Despite its limitations, the CCDD rectifier remains widely used in many energy harvesting systems due to its simplicity and effectiveness.

In [10], an adaptive-biasing technique is proposed to supply bias current to the gate of the PMOS transistor, thereby limiting power loss at high input power levels. However, the complexity of the bias circuit restricts its impact, as it only addresses power consumption in the PMOS. In [8,11], a diode-connected structure is introduced as a bias circuit for double-sided rectifiers, which effectively reduces the rectifier's power consumption, achieving a peak PCE of 86%. In [12], a stacking diode structure is employed to bias the NMOS transistor, resulting in significant reduction in power consumption at high input power levels. Additionally, in [13], an adaptive-biasing technique is used to reduce the threshold voltage of MOS transistors, leading to a dynamic range of 14.5 dB.

This paper presents a LCS technique that effectively mitigates reverse leakage current under high input power, thereby improving the

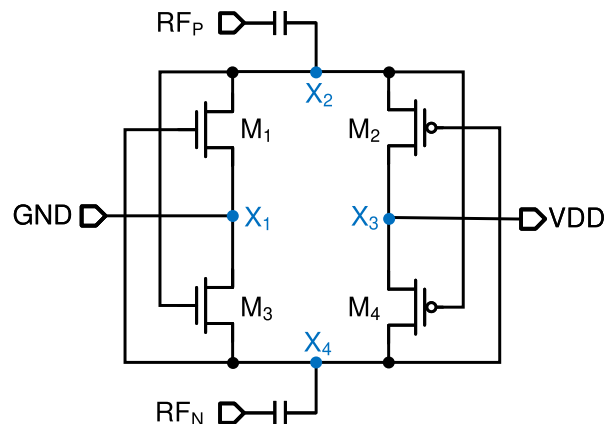


**Fig. 3.** Schematic of the Cross-Coupled Differential Drive (CCDD) rectifier.

dynamic range of the rectifier. Additionally, adaptive-biasing techniques are applied to the gate, leading to a significant enhancement in the PCE of the rectifier. The application of dynamic substrate biasing on the PMOS substrate further reduces the effective threshold voltage, thereby improving the rectifier's sensitivity. The structure of the paper is as follows: Section 2 analyzes the factors contributing to the decline in power transfer efficiency in conventional rectifiers. Section 3 introduces the proposed rectifiers and presents the corresponding simulation results. Section 4 provides a conclusion.

## 2. Technical analysis

The CCDD rectifier is shown in Fig. 3. The device is capable of achieving high sensitivity and high PCE, although it is worth noting that its performance may be limited to a narrow input power range. We designed a CCDD-structured rectifier using a TSMC 40 nm process for simulation and analysis. To compare the proposed rectifier, a 200 k $\Omega$  resistor was used as the load.

Since impedance matching network design is not considered in this study, the actual power absorbed by the rectifier, denoted as  $P_{abs}$ , must be determined to accurately evaluate its PCE. This is accomplished by measuring the input reflection coefficient ( $S_{11}$ ) and calculating the absorbed power as:

$$P_{abs} = P_{inc} (1 - |S_{11}|^2) \quad (1)$$

where  $P_{inc}$  is the incident power delivered by the source,  $|S_{11}|$  is the magnitude of the reflection coefficient at the operating frequency,  $|S_{11}|^2$  represents the fraction of incident power that is reflected due to impedance mismatch [14].

As shown in Fig. 4, the peak PCE of 76.8% is achieved at an input power level of -27.2 dBm. However, the PCE gradually decreases with increasing input power due to the rise in reverse leakage current.

The next part will analyze the reasons for the decrease in PCE under high input power conditions.

Fig. 5 shows the transient voltage and current waveforms of the NMOS transistors (M1, M3) at  $P_{abs} = -25$  dBm. One operating cycle exhibits both forward and reverse conduction regions. As  $V_S > V_D$ , the MOSFET enters the cutoff region when  $V_{GD} \ll V_{TH}$ . The reverse leakage current in this region is approximately 31 nA, which can be considered negligible. As  $V_{GD}$  increases, the device transitions from the cutoff region into the subthreshold region.

The drain current of an NMOS transistor operating in the subthreshold region can be expressed as:

$$I_D = I_0 \cdot \exp\left(\frac{V_{GS} - V_{th}}{n \cdot U_T}\right) \cdot \left(1 - \exp\left(-\frac{V_{DS}}{U_T}\right)\right) \quad (2)$$

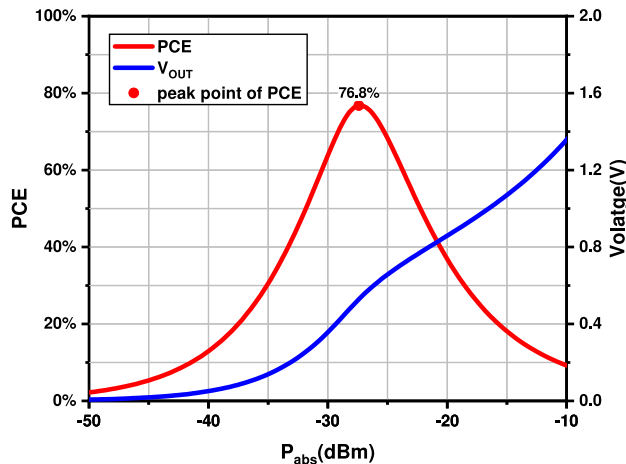


Fig. 4. Simulated PCE of the CCDD rectifier versus  $P_{abs}$  at a load of 200 k $\Omega$ .

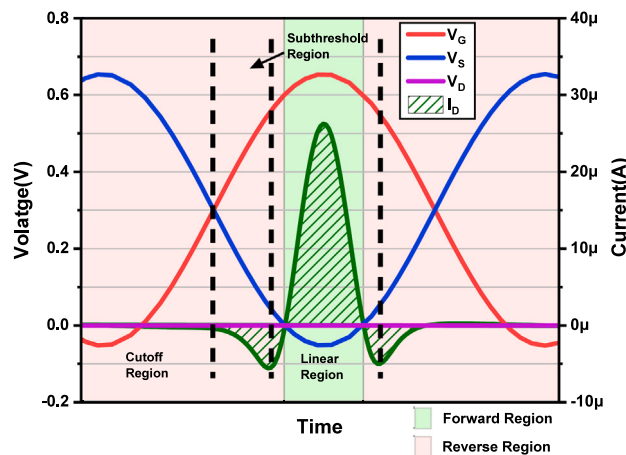


Fig. 5. Transient waveform of NMOS transistor ( $M_1, M_3$ ) within one operating cycle at  $P_{abs} = -25$  dBm.

where  $I_0$  is a device-dependent current coefficient incorporating process and geometric parameters,  $n$  is the subthreshold swing factor, and  $U_T$  is the thermal voltage. For  $V_{DS} > 3U_T$ , the exponential term  $(1 - \exp(-V_{DS}/U_T))$  approaches unity, resulting in a simplified expression:

$$I_D = I_0 \cdot \exp\left(\frac{V_{GS} - V_{TH}}{n \cdot U_T}\right) \quad (3)$$

When  $V_D > V_S$ , the MOSFET operates in the forward conduction mode and remains in the linear region. The drain current  $I_D$  in the linear region of a MOSFET is given by:

$$I_D = k' \left( \frac{W}{L} \right) \left[ (V_{GS} - V_{th}) V_{DS} - \frac{V_{DS}^2}{2} \right] \quad (4)$$

where  $I_D$  denotes the drain current,  $k'$  is a process-dependent transconductance parameter,  $W$  and  $L$  are the channel width and length of the MOSFET, respectively,  $V_{GS}$  is the gate-to-source voltage,  $V_{th}$  is the threshold voltage, and  $V_{DS}$  is the drain-to-source voltage.

Fig. 5 shows that the NMOS transistor enters the reverse conduction region twice within one operating cycle. The peak reverse and forward currents are 5.3  $\mu$ A and 25  $\mu$ A, respectively. This indicates that the reverse leakage current is non-negligible.

The PMOS transistor ( $M_2, M_4$ ) will also exhibit reverse leakage current. In the CCDD structure, the alternating conduction of NMOS and PMOS transistors causes the RF port capacitance to alternate between

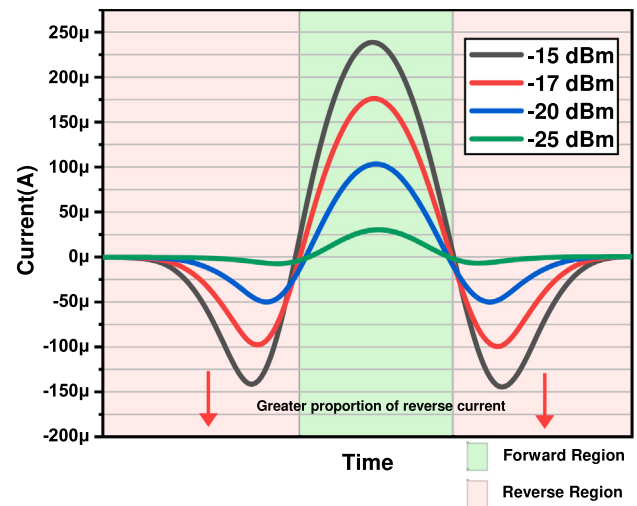


Fig. 6. Simulated current through NMOS transistor ( $M_1, M_3$ ) at different input powers within one operating cycle.

charging and discharging states. This alternation ultimately allows the current to flow from GND to the VDD port, completing the RF to DC conversion.

It is well known that PCE is significantly influenced by reverse leakage current [14]. Fig. 6 shows the transient conduction current of the NMOS transistor ( $M_1, M_3$ ) tested under different input power levels. As the input power increases from -25 dBm, the proportion of reverse leakage current gradually increases, leading to a gradual decrease in PCE. The results are consistent with the PCE curve shown in Fig. 4.

Since the forward current through the rectifier is an inevitable consequence of its operation, one approach to enhancing the PCE of the rectifier is to reduce the proportion of reverse leakage current in the total current over a single cycle. In order to more accurately represent the impact of reverse leakage current on PCE, it can be represented by measuring the power consumption of MOSFETs. Fig. 7 shows the power consumption of the MOSFETs when the rectifier's output voltage reaches 1 V. The data indicates that the peak power consumption of the NMOS is 20  $\mu$ W, while that of the PMOS is 10  $\mu$ W. In comparison, the load resistor consumes only 5  $\mu$ W at this point. The MOSFETs consume most of the power, causing the PCE in this state to drop to 22.5% (Fig. 4). The large drain-to-source voltage differential during reverse leakage current significantly increases the power consumption. Specifically, the power dissipated due to reverse leakage current is approximately twice that of the forward conduction current.

Based on the power consumption analysis of the MOSFETs, two effective strategies to improve PCE are identified:

1. Reducing the proportion of reverse current during the MOSFET's operation cycle.
2. Minimizing the drain-source voltage  $V_{DS}$  of the MOSFETs.

This work enhances the PCE by decreasing the MOSFET's power consumption during rectifier operation through the mitigation of reverse leakage current and partial excess forward current.

### 3. Proposed design

#### 3.1. Proposed LCS-R1

Fig. 8 illustrates the proposed LCS-R1. It employs the leakage-current-suppressing (LCS) technique. Depletion-type NMOS transistors configured in a diode-connected structure are added to both the DC

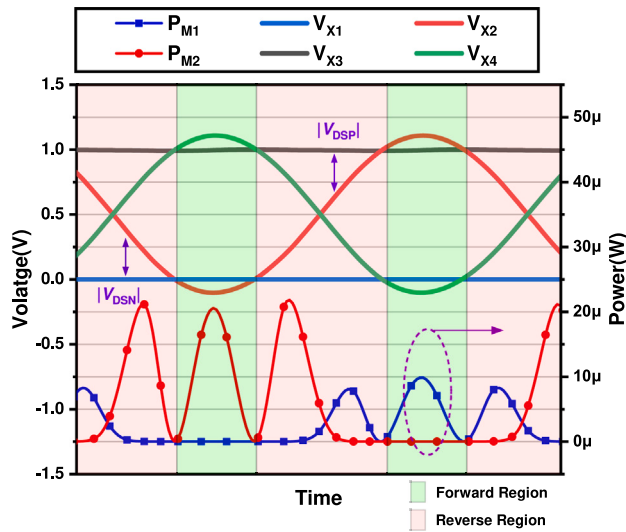


**Fig. 7.** Transient waveforms of MOSFETs voltage and power consumption in the CCDD rectifier at  $V_{\text{OUT}} = 1 \text{ V}$ .

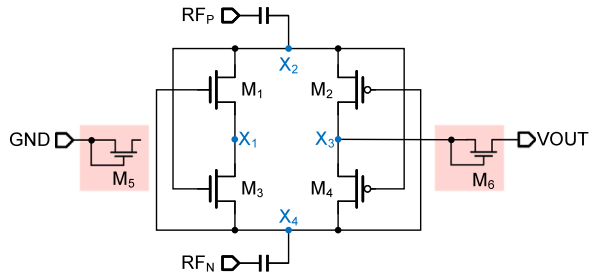


**Fig. 8.** Schematic of the proposed LCS-R1.

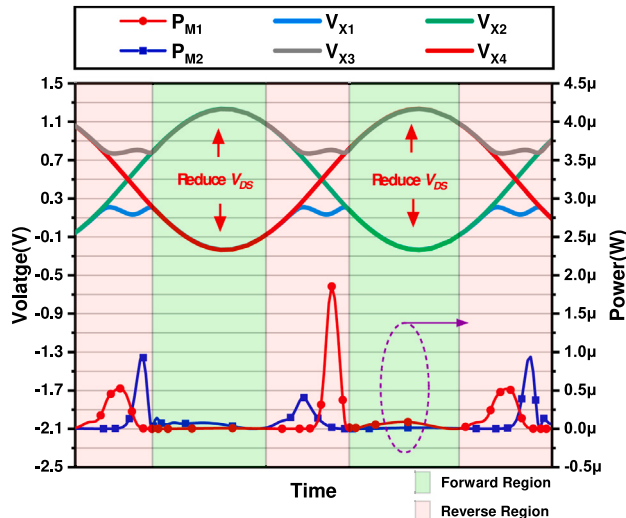


**Fig. 9.** Transient waveforms of MOSFET voltage and power consumption in the LCS-R1 at  $V_{\text{OUT}} = 1 \text{ V}$ .

voltage input and output ends of the rectifier. The use of depletion-type NMOS transistors ensures proper conduction at both the input and output ports even under low input power conditions, thereby maintaining high sensitivity. This circuit structure effectively reduces the reverse leakage current in the main MOS transistors ( $M_1$ - $M_4$ ), while also lowering their drain-source voltage  $V_{DS}$  during conduction.

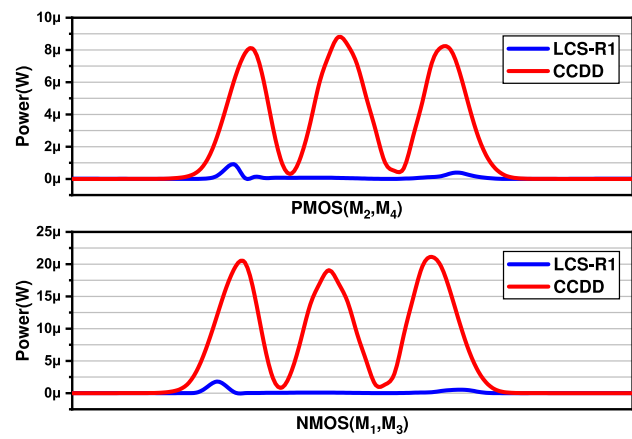


**Fig. 10.** Transient power consumption of the main transmission MOSFETs ( $M_1$ - $M_4$ ) over one operating cycle in the CCDD and LCS-R1 at  $R_L = 200 \text{ k}\Omega$  and  $V_{\text{OUT}} = 1 \text{ V}$ .

**Fig. 9** shows the internal node voltages ( $X_1$ - $X_4$ ) of the LCS-R1 rectifier at 1 V output voltage, as well as the power consumption of MOSFETs  $M_1$  and  $M_2$ . Unlike the CCDD rectifier, the voltage at node  $X_1$  and  $X_3$  is not fixed.

As the voltage at node  $V_{X_2}$  decreases and  $V_{X_4}$  increases, MOSFET  $M_1$  turns on, leading to a rise in  $I_{M_1}$ . At this stage,  $M_3$  remains in cutoff, resulting in  $I_{M_1} = I_{M_5}$ . The increase in  $I_{M_1}$  raises the drain-source voltage  $V_{DS,M_5}$  of  $M_5$ , which in turn causes a voltage drop at node  $X_1$ , as shown in **Fig. 9**. This voltage drop at  $X_1$  reduces  $V_{DS,M_1}$ , thereby limiting the current  $I_{M_1}$  and suppressing excessive power dissipation in  $M_1$ . Similarly, when  $V_{X_2}$  rises and  $V_{X_4}$  falls,  $M_3$  and  $M_5$  conduct, synchronizing the voltage at  $X_1$  with  $V_{X_4}$ . Therefore,  $M_5$  effectively suppresses the excess forward conduction current of  $M_1$  and  $M_3$ , thereby reducing the power loss during conduction. Similarly, the LCS circuit at the output increases the voltage at node  $X_3$  during forward conduction, thereby reducing the power dissipation of the PMOS transistor in its forward conduction state.

Similar to the limitation of forward current, when reverse leakage current occurs in  $M_5$ , the voltage at node  $V_{X_1}$  rises in response to the dynamic increase at nodes  $V_{X_2}$  or  $V_{X_4}$ , thereby reducing the  $V_{DS}$  of  $M_1/M_3$ . For the depletion-type NMOS transistor  $M_5$ ,  $V_{GS} = 0 \text{ V}$ . When  $V_{DS} > -V_{TH}$ , the NMOS enters saturation. With  $V_{TH} = -195 \text{ mV}$ , the depletion-type NMOS can effectively suppress reverse leakage current even at moderate input power levels.

Since the node voltages  $V_{X_1}$  and  $V_{X_3}$  dynamically change with the direction of current flow, the LCS technique significantly suppresses both forward and reverse conduction losses. **Fig. 10** shows a comparison of the power consumption in the MOSFETs of the proposed LCS-R1 and the CCDD.

As shown in **Fig. 9**, the LCS technique enables the main transmission MOSFETs ( $M_1$ - $M_4$ ) to operate with an extremely low  $V_{DS}$ , resulting in minimal power consumption. However, implementing the LCS technique requires precise adjustment of the width-to-length ratios ( $W/L$ ) of MOSFETs  $M_5$  and  $M_6$ . Otherwise, the dynamic range extension capability of the rectifier cannot be effectively achieved. **Fig. 11** compares the dynamic range extension performance of the LCS structure across varying width-to-length ( $W/L$ ) ratios of the MOSFETs. It is evident that an inappropriate  $W$  value can degrade either the PCE or the dynamic range. Therefore, a proper  $W$  value should be estimated during the design of the LCS structure.

Under steady-state operation of the rectifier, the DC level at node  $X_2$  stabilizes at approximately half the output voltage ( $V_{X_2} = \frac{1}{2}V_{\text{OUT}}$ ). Given  $V_{RFP} = -V_{RF}$ , this condition leads to  $V_{X_2} = \frac{1}{2}V_{\text{OUT}} - V_{RF}$ . Due to the negligible  $V_{DS}$  of  $M_1$ , we can approximate  $V_{X_1} \approx V_{X_2}$ . Since

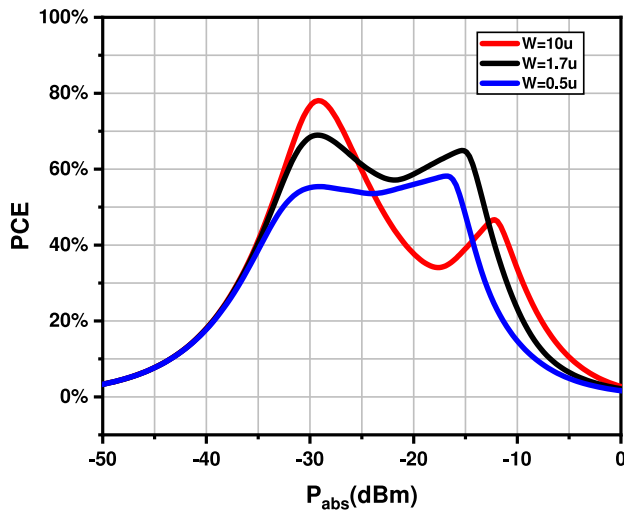


Fig. 11. PCE of MOSFETs (M5, M6) with varying W/L ratios.

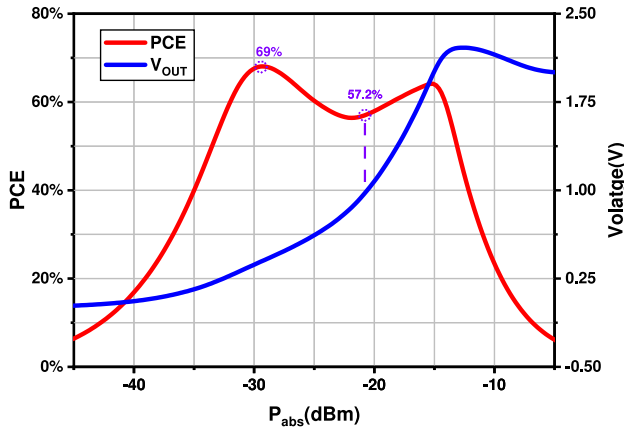


Fig. 12. Simulated PCE and  $V_{OUT}$  versus  $P_{abs}$  for the LCS-R1 with  $R_L = 200$  k $\Omega$ .

depletion-type NMOS transistors have  $V_{TH} < 0$ , for  $M_5$  we derive  $V_{DS} < V_{GS} - V_{TH}$ , placing it in the linear region. With  $V_{GS} = V_{DS} = V_{RF} - \frac{1}{2}V_{OUT}$ , the forward conduction current of  $M_5$  is obtained from (4) as:

$$\begin{aligned} I_D &= k' \frac{W}{L} \left( \frac{V_{DS}^2}{2} - V_{th} V_{DS} \right) \\ &= k' \frac{W}{L} \left[ \frac{(V_{RF} - \frac{1}{2}V_{OUT})^2}{2} - V_{th}(V_{RF} - \frac{1}{2}V_{OUT}) \right] \\ &= k' \frac{W}{L} \left( \frac{1}{8}V_{OUT}^2 + \frac{1}{2}(V_{th} - V_{RF})V_{OUT} \right. \\ &\quad \left. + \frac{1}{2}V_{RF}(V_{RF} - 2V_{th}) \right) \end{aligned} \quad (5)$$

From Fig. 9, approximately 50% of the operating cycle shows  $M_5$  conduction, leading to the estimation  $I_{D,M5} \approx 2I_{OUT}$ . Substituting into (5), we derive:

$$\begin{aligned} k' \frac{W}{L} &= \frac{2V_{OUT}}{R_L \left[ \frac{1}{8}V_{OUT}^2 + \frac{1}{2}(V_{th} - V_{RF})V_{OUT} + \frac{1}{2}V_{RF}(V_{RF} - 2V_{th}) \right]} \\ &= \frac{16V_{OUT}}{R_L \left[ V_{OUT}^2 + 4(V_{th} - V_{RF})V_{OUT} + 4V_{RF}(V_{RF} - 2V_{th}) \right]} \end{aligned} \quad (6)$$

Using design parameters  $V_{OUT} = 1$  V,  $R_L = 200$  k $\Omega$ , and  $V_{RF} = 0.6$  V (slightly higher than  $\frac{1}{2}V_{OUT}$ ), process data yields  $k' = 275.72 \mu\text{A/V}^2$  and

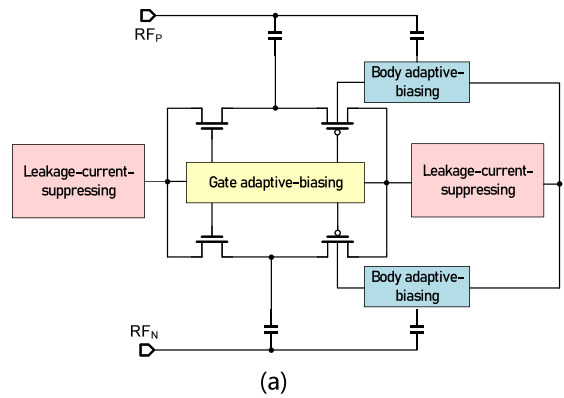


Fig. 13. (a)-The proposed architecture, (b)-Schematic of the proposed LCSAB-R2 rectifier.

$V_{TH} = -195$  mV. Eq. (6) gives  $W/L = 1.48$ , leading to  $W = 1.776 \mu\text{m}$  for  $L = 1.2 \mu\text{m}$ . Improper  $W/L$  selection for the LCS MOSFETs compromises the wide-dynamic-range performance. Excessive  $W$  increases the main MOSFETs'  $V_{DS}$  (no longer negligible), raising power consumption and degrading PCE at high input powers. Conversely, insufficient  $W$  limits the current supply capability of  $M_5/M_6$  at low input levels, reducing rectifier sensitivity. Therefore, moderate  $W$  values are critical for optimal LCS performance.

The proposed LCS technique effectively minimizes the power dissipation of the main rectifying transistors ( $M_1$ - $M_4$ ), shifting the primary source of power consumption to the LCS structure ( $M_5$  and  $M_6$ ). This technique addresses the issue of reduced PCE in CCDD topology under high input power conditions, thereby expanding the power dynamic range (PDR) of the rectifier.

Fig. 12 shows the PCE and output voltage  $V_{OUT}$  of the LCS-R1 versus actual absorbed power  $P_{abs}$ . At a frequency of 433 MHz and a load of 200 k $\Omega$ , the peak PCE of the LCS-R1 achieves 69%. The dynamic range for PCE greater than 40% is 22.9 dB, spanning from -35.0 dBm to -12.1 dBm. The input power required to achieve  $V_{OUT} = 1$  V is -20.6 dBm, which is a 4 dB improvement compared to the CCDD rectifier.

When the output voltage is 1 V, the proposed LCS-R1 rectifier achieves a peak efficiency of 57.2%, while the PCE of the conventional CCDD rectifier is 24.2%. Although the LCS-R1 exhibits a 7.8% degradation in peak PCE at low input power levels due to the additional two NMOS transistors, its key advantages lie in the extended dynamic range and improved sensitivity. Specifically, the power dynamic range with  $PCE > 40\%$  is extended by 10.2 dB, and the sensitivity is enhanced by 4.1 dB simultaneously. The wider dynamic range enables the rectifier to provide stable output in complex electromagnetic environments.

The LCS technique demonstrates pronounced advantages under high input power conditions. Although the LCS structure itself incurs power dissipation, its power consumption remains relatively low in the high-power regime. Meanwhile, this technique achieves a net gain in overall

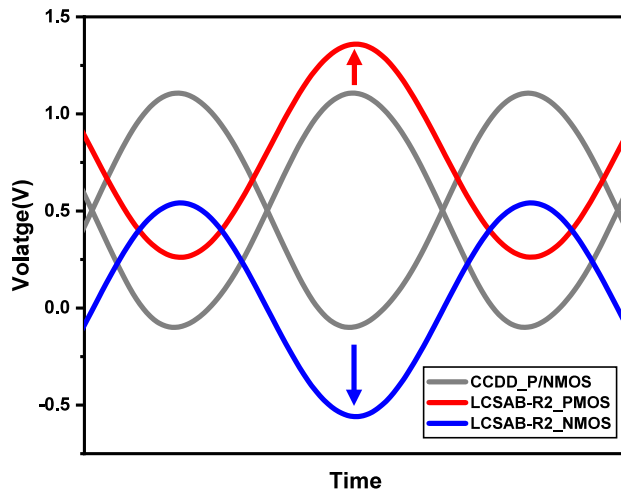


**Fig. 14.** Transient waveforms of the MOSFET gate voltage in the LCSAB-R2 and CCDD rectifiers at  $V_{\text{OUT}} = 1 \text{ V}$ .

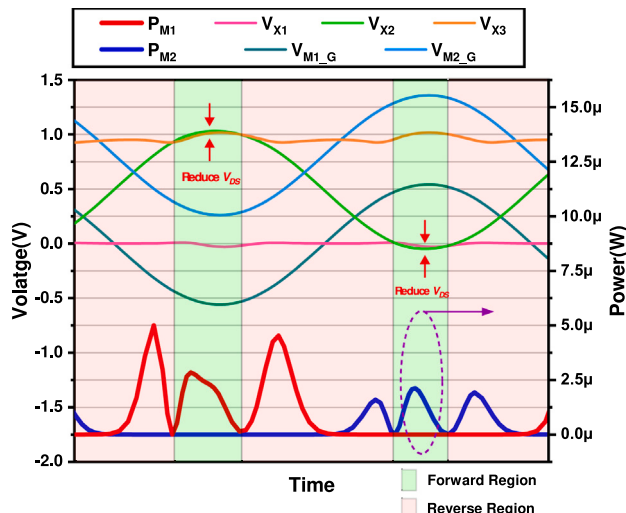


**Fig. 15.** Transient power consumption of the MOSFET over one operating cycle in the CCDD and LCSAB-R2 rectifiers at  $R_L = 200 \text{ k}\Omega$  and  $V_{\text{OUT}} = 1 \text{ V}$ .

PCE by dynamically suppressing the power dissipation of the main transmission MOSFETs ( $M_1$ - $M_4$ ). This characteristic makes LCS-R1 particularly suitable for high-power-density applications.

### 3.2. Proposed LCSAB-R2

The LCSAB-R2 topology, based on the integration of leakage-current suppression and adaptive-biasing techniques, incorporates gate adaptive-biasing circuits, as shown in Fig. 13.

The integration of adaptive-biasing circuits is primarily aimed at reducing the overdrive voltage of the main transmission MOSFETs ( $M_1$ - $M_4$ ) under high input power conditions, which in turn suppresses reverse leakage current and minimizes additional power consumption from forward current. To ensure that the gate voltage biasing does not impede the normal operation of the rectifier, capacitors  $C_3$  -  $C_6$  are employed to directly couple the RF signal to the gate of the MOS transistors. Diodes  $D_1$  to  $D_4$  are utilized to furnish DC biasing for the gate voltage, with the notable distinction that the biasing diodes for NMOS( $M_1, M_3$ ) and PMOS( $M_2, M_4$ ) transistors exhibit opposing orientations. This discrepancy arises from the necessity to diminish the gate voltage for NMOS transistors while elevating it for PMOS transistors

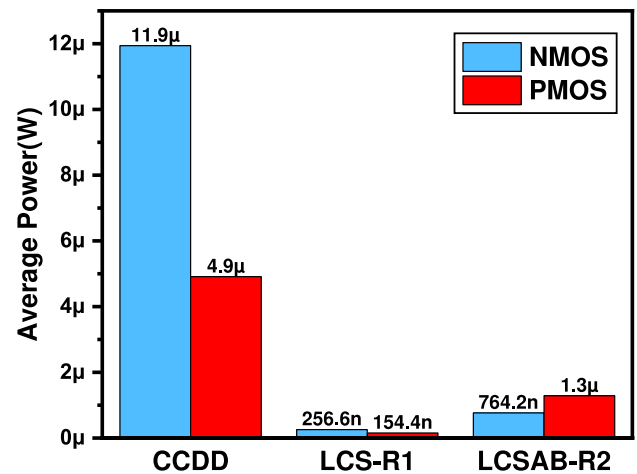


**Fig. 16.** Average power consumption of the MOSFET in the proposed rectifiers and the CCDD rectifier at  $V_{\text{OUT}} = 1 \text{ V}$  and  $R_L = 200 \text{ k}\Omega$ .

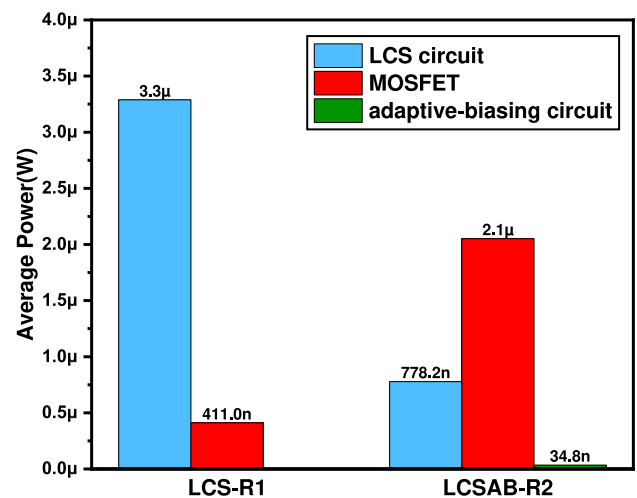


**Fig. 17.** Average power consumption in the Leakage-current-suppressing and adaptive-biasing circuits at  $V_{\text{OUT}} = 1 \text{ V}$  and  $R_L = 200 \text{ k}\Omega$ .

to minimize MOS transistor power consumption under high-power input conditions. Additionally, the adaptive-biasing circuit ( $D_5$ ,  $D_6$ ) is integrated into the substrate of the PMOS transistor to reduce its threshold voltage and enhance the sensitivity of the rectifier [15].

With the adaptive-biasing circuit connected to the gates of  $M_1$  to  $M_4$ , at low RF power levels, the voltage drop across the diodes is less than the threshold voltage, causing the diodes to behave as open circuits. Consequently, the gate voltages of  $M_1$  to  $M_4$  are effectively directly connected to the RF nodes, reconfiguring the rectifier to a CCDD circuit.

For input power levels in the medium to high range, when the voltage drop across diodes  $D_1$  to  $D_4$  exceeds the threshold voltage, the diodes become forward-biased. In this state,  $D_2$  and  $D_1$ , respectively, reduce the gate voltage of  $M_1$  and  $M_3$ , while  $D_4$  and  $D_3$ , respectively, increase the gate voltage of  $M_2$  and  $M_4$ . This results in the superposition of the RF signal on a DC bias voltage. Fig. 14 compares the transient gate voltages of the CCDD and adaptive-biasing circuits at an output voltage of 1 V. It shows that the NMOS gate voltage in the adaptive-biasing circuit is lower than that in the CCDD rectifier, while the PMOS gate voltage is higher.

In the CCDD rectifier, for the NMOS transistor  $M_1$ , the proportion of time within a cycle when the gate-source voltage ( $V_{GS}$ ) is greater

**Table 1**

Design parameters of the proposed rectifiers.

| Gate dimensions ( $\mu\text{m}$ ) | $M_1$  | $M_2$   | $M_3$  | $M_4$   | $M_5-M_6$ | $D_1-D_4$ | $D_5-D_6$ |
|-----------------------------------|--------|---------|--------|---------|-----------|-----------|-----------|
| LCS-R1                            | 3/0.04 | 8/0.04  | 3/0.04 | 8/0.04  | 1.7/1.2   | —         | —         |
| LCSAB-R2                          | 6/0.04 | 10/0.04 | 6/0.04 | 10/0.04 | 50/1.2    | 2.8/2.8   | 0.5/0.5   |

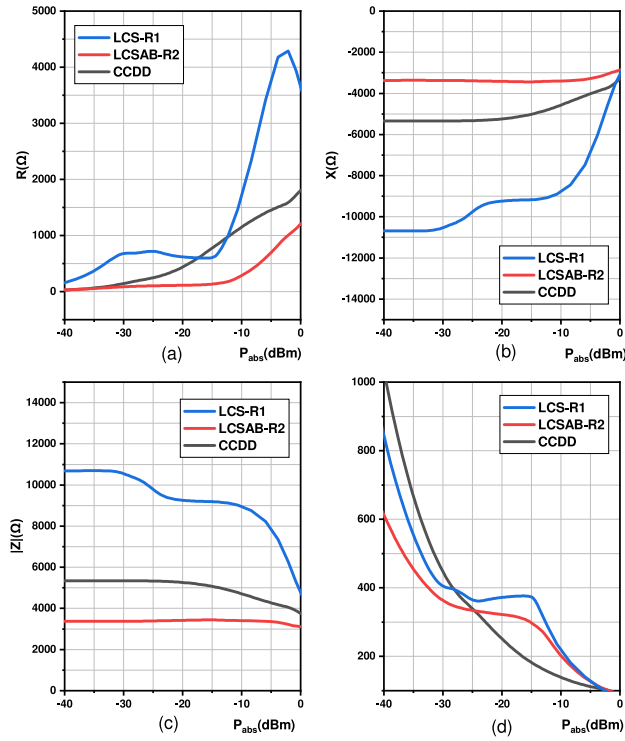


Fig. 18. Input impedance characteristics of the rectifiers: (a) input resistance, (b) input reactance, (c) magnitude of the input impedance, and (d) the coefficient  $K$  derived from the input impedance.

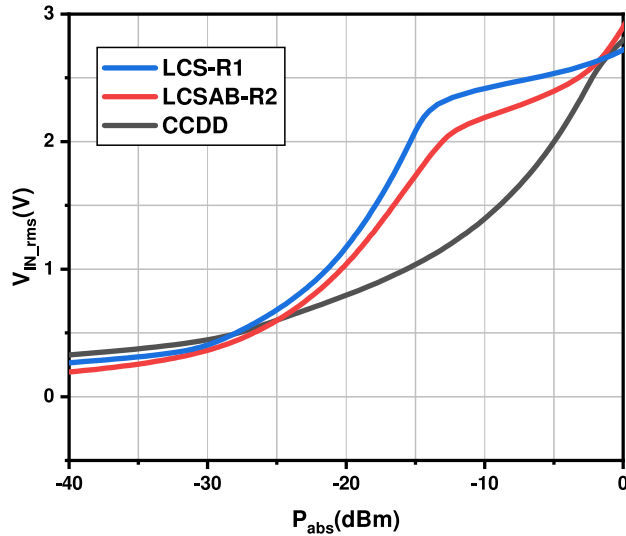


Fig. 19. Simulated input RMS voltage  $V_{\text{in},\text{rms}}$  versus absorbed power  $P_{\text{abs}}$ .

than zero is 50%. However, with the adoption of the adaptive-biasing technique, the gate voltage is superimposed with a negative DC voltage, resulting in a  $V_{\text{GS}}$  greater than zero for less than 50% of the time. The reduction in the proportion of time during which  $V_{\text{GS}} > 0$  directly corresponds to a shorter forward conduction period for  $M_1$ . Under high input

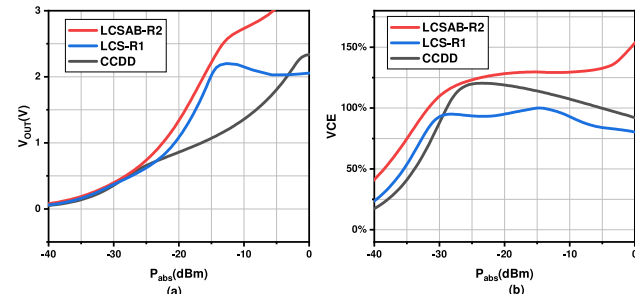


Fig. 20. (a) Simulated output voltage  $V_{\text{out}}$  versus absorbed power  $P_{\text{abs}}$ . (b) Simulated voltage conversion efficiency (VCE) versus  $P_{\text{abs}}$ .

power conditions, a very short conduction time is sufficient to provide adequate forward current to the load. Therefore, reducing the forward conduction time of the MOS transistor within a cycle can significantly minimize additional forward power consumption. This phenomenon is one of the reasons why the PCE of the traditional CCDD rectifier decreases under high power input conditions. For the PMOS transistor, the increased gate voltage due to the adaptive-biasing circuits also shortens its conduction time within a cycle. The adaptive-biasing circuits dynamically adjusts the gate voltage of the MOS transistor based on the current output voltage, thereby controlling the conduction time of the MOS transistor within an optimal range. This adjustment not only suppresses the reverse leakage current but also reduces the power consumption of the forward current.

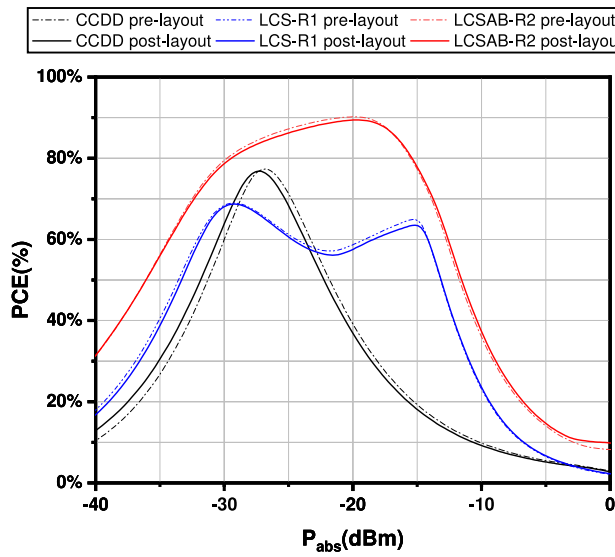
Fig. 15 shows the internal node voltages and MOSFET power consumption of the LCSAB-R2 during operation. As shown in the figure, the LCS technique effectively reduces the  $V_{DS}$  of the main MOSFETs, while the adaptive-biasing technique enables dynamic gate voltage adjustment beyond the LCS-R1 architecture. This dual-optimization strategy achieves a higher PCE and extends the power dynamic range.

Fig. 16 presents the simulated average power consumption of the main transmission MOSFETs in the three rectifier architectures at  $V_{\text{OUT}} = 1$  V. Comparative analysis confirms that the LCS technique significantly reduces the power consumption of the main MOSFETs, from 16.8  $\mu\text{W}$  in the CCDD rectifier to 0.411  $\mu\text{W}$  in the LCS-R1. Fig. 16 presents the simulated average power consumption of the main transmission MOSFETs in the three rectifier architectures at  $V_{\text{OUT}} = 1$  V.

It is noted that the power consumption of MOS transistors in LCS-R1 is lower than that of the LCSAB-R2. However, its PCE is still lower than that of the LCSAB-R2. Fig. 17 compares the components of power consumption between the LCS-R1 and LCSAB-R2. The figure indicates that the addition of adaptive-biasing circuits significantly reduces the power consumption of the LCS circuit itself. Moreover, the power consumption of the adaptive-biasing circuits is negligible, resulting in a higher overall PCE for the LCSAB-R2 compared to the LCS-R1.

The LCSAB-R2 improves upon LCS-R1 by modifying the main rectifier architecture, demonstrating that the LCS technique can be reused in other advanced rectifiers to enhance dynamic range. Although LCS may introduce additional power consumption, future work could explore enabling the LCS structure only when needed — e.g., based on input power detection — to avoid unnecessary overhead.

Table 1 summarizes the gate dimensions (width-to-length ratios) of the transistors and diodes.



**Fig. 21.** Simulated PCE versus  $P_{\text{abs}}$  for LCS-R1, LCSAB-R2, and CCDD at  $f = 433 \text{ MHz}$  and  $R_L = 200 \text{ k}\Omega$ .

### 3.3. Simulation results

To evaluate the rectifier's true performance, an ideal matching network is employed in this work. Under the same actual received power  $P_{\text{abs}}$ , the input voltage  $V_{\text{in}}$  is determined by the rectifier's input impedance. Based on the relation

$$P_{\text{abs}} = I_{\text{in,rms}}^2 R, \quad (7)$$

where  $I_{\text{in,rms}} = V_{\text{in,rms}} / |Z|$ , we rearrange to obtain

$$V_{\text{in,rms}} = \sqrt{P_{\text{abs}} \cdot \frac{|Z|^2}{R}}. \quad (8)$$

To quantify the impact of impedance on the input voltage, we define an empirical coefficient:

$$K = \sqrt{\frac{|Z|^2}{R}}, \quad (9)$$

so that

$$V_{\text{in,rms}} = \sqrt{P_{\text{abs}}} \cdot K. \quad (10)$$

The post-layout input impedance  $Z = R + jX$  of the rectifier is extracted via large-signal impedance analysis using harmonic balance (HB) simulation. The simulation results are shown in Fig. 18.

The calculated empirical coefficient  $K$  is shown in Fig. 18(d). For  $P_{\text{abs}} > -25 \text{ dBm}$ , the  $K$ -values of the LCS-R1 and LCSAB-R2 rectifiers exceed that of the CCDD rectifier. Since  $V_{\text{in,rms}}$  is proportional to  $K$ , the input RMS voltages of the LCS-R1 and LCSAB-R2 rectifiers are correspondingly higher than that of the CCDD rectifier under the same  $P_{\text{abs}}$ . The simulated  $V_{\text{in,rms}}$  results are presented in Fig. 19.

The ability of a rectifier to convert input voltage into output voltage can be quantified by the voltage conversion efficiency (VCE) [16], defined as:

$$\text{VCE} = \frac{V_{\text{out}}}{V_{\text{in,rms}}}. \quad (11)$$

The simulated VCE and output voltage  $V_{\text{out}}$  of the proposed rectifiers are shown in Fig. 20. The LCSAB-R2 achieves a higher VCE than the LCS-R1, which implies that it can deliver a larger  $V_{\text{out}}$  even when its  $V_{\text{in,rms}}$  is smaller than that of the LCS-R1.

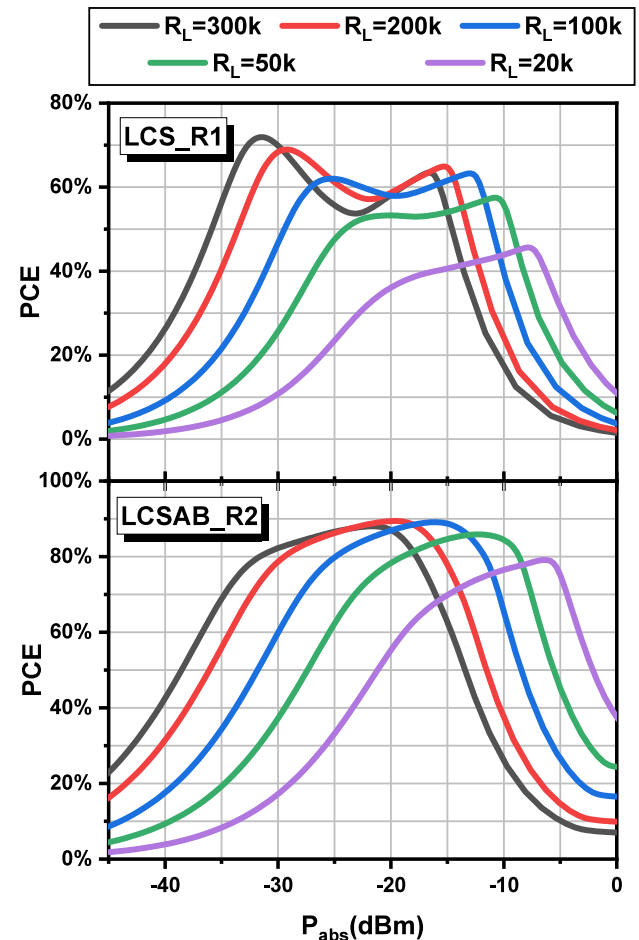


**Fig. 22.** Load-dependent PCE versus  $P_{\text{abs}}$  under varying load conditions ( $R_L = 20 \text{ k}\Omega$  to  $300 \text{ k}\Omega$ ).

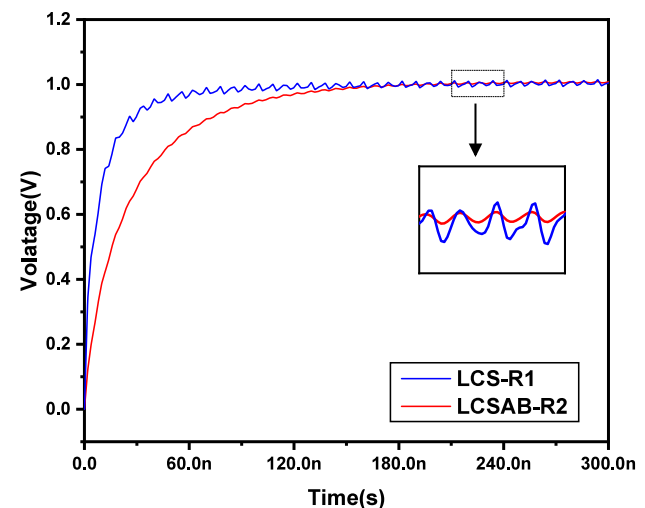


**Fig. 23.** Transient output voltage waveforms for the proposed rectifiers with  $V_{\text{out}} = 1 \text{ V}$ .

The power conversion efficiency is defined as:

$$\text{PCE} = \frac{P_{\text{out}}}{P_{\text{abs}}} \times 100\% \quad (12)$$

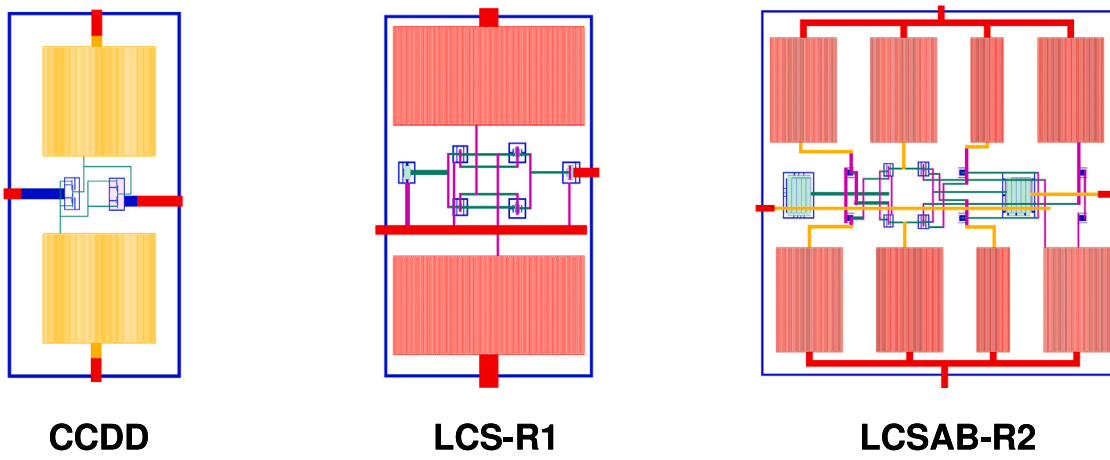


**Fig. 24.** Layouts of the three rectifiers in 40 nm CMOS technology. Active areas: LCSAB-R2 ( $0.12 \text{ mm}^2$ ), LCS-R1 ( $0.09 \text{ mm}^2$ ), CCDD ( $0.07 \text{ mm}^2$ ).

**Table 2**  
Comparison with state-of-the-art works.

| Ref.      | Topology                       | Technology | Frequency | Load resistance | Peak PCE (%)                  | Dynamic range (dBm)@PCE>40%   | Sensitivity (dBm)@1V                |
|-----------|--------------------------------|------------|-----------|-----------------|-------------------------------|-------------------------------|-------------------------------------|
| This work | LCSAB                          | 40 nm      | 433 MHz   | 200 k $\Omega$  | 89.4 @ -19.7 dBm              | -38.0 to -10.3                | -22.5                               |
|           | LCS                            |            |           |                 | 69 @ -29.3 dBm                | -35.0 to -12.1                | -20.6                               |
|           | CCDD                           |            |           |                 | 76.8 @ -27.2 dBm              | -33.3 to -20.6                | -16.5                               |
| [19]'2025 | Dynamically biased             | 65 nm      | 915 MHz   | 7 k $\Omega$    | 80 <sup>a,b</sup> @ 0 dBm     | -17 to 6 <sup>a,b</sup>       | -7 @ 7 k $\Omega$ <sup>a,b</sup>    |
| [20]'2025 | Dual Gate & Body Self-Biasing  | 180 nm     | 920 MHz   | 100 k $\Omega$  | 78.5 <sup>b</sup> @ -18.7 dBm | -28.5 to -12 <sup>a,b</sup>   | -18.9 @ 100 k $\Omega$ <sup>b</sup> |
| [21]'2024 | 1-stage CCLC                   | 65 nm      | 2.4 GHz   | 500 $\Omega$    | 70 <sup>a,b</sup> @ 0 dBm     | -7.5 to 10 <sup>a</sup>       | -3 @ 1 M $\Omega$                   |
| [22]'2023 | ALL-NMOS                       | 180 nm     | 200 MHz   | 10 k $\Omega$   | 57.6 @ -13.78 dBm             | -17 to -8 <sup>a</sup>        | -14.8 @ 1 M $\Omega$                |
| [14]'2023 | Advanced topology amalgamation | 65 nm      | 900 MHz   | 100 k $\Omega$  | 79.77 @ -17.5 dBm             | -23 to -10 <sup>a</sup>       | -15.5 @ 100 k $\Omega$              |
| [23]'2023 | Dual-Topology                  | 130 nm     | 900 MHz   | 100 k $\Omega$  | 89 <sup>a,b</sup> @ -16 dBm   | -20 to -5 <sup>a,b</sup>      | -17.7 @ $\infty$ $\Omega$           |
| [24]'2022 | DDCCB                          | 130 nm     | 953 MHz   | 50 k $\Omega$   | 75.7 <sup>b</sup> @ -11 dBm   | -14 to -3 <sup>a,b</sup>      | -14 @ 50 k $\Omega$ <sup>a,b</sup>  |
| [25]'2021 | ICC                            | 130 nm     | 900 MHz   | 100 k $\Omega$  | 80.3 @ -17 dBm                | -22.5 to -8                   | -18.7 @ 100 k $\Omega$              |
| [26]'2020 | DM                             | 65 nm      | 433 MHz   | 100 k $\Omega$  | 86 @ -20 dBm                  | -35 to -14 <sup>a</sup>       | -19.2 @ 100 k $\Omega$              |
| [27]'2018 | DTMOS CCDD                     | 130 nm     | 915 MHz   | 300 k $\Omega$  | 81.55 <sup>b</sup> @ -32 dBm  | -36.8 to -22.2 <sup>a,b</sup> | -                                   |

<sup>a</sup> Estimated from the figure.

<sup>b</sup> Simulation results are reproduced in this work.

where  $P_{\text{out}}$  is the DC output power and  $P_{\text{abs}}$  denotes the absorbed RF power.

Power dynamic range (PDR) is another important performance metric for rectifiers. The PDR, characterizing the operational power window with PCE above a specified threshold (e.g., 40% or 80% of peak PCE) [17,18]. Mathematically, it is expressed as:

$$\text{PDR (dB)} = P_{\max} (\text{dBm}) - P_{\min} (\text{dBm}) \quad (13)$$

where  $P_{\max}$  and  $P_{\min}$  represent the maximum and minimum input power levels, respectively, at which the rectifier sustains PCE above the designated threshold value.

Fig. 21 shows both pre- and post-layout PCE results for the three circuits, simulated at 433 MHz with a 200 k $\Omega$  load. The reported performance metrics correspond to post-layout simulations. The proposed LCSAB-R2 achieves a peak PCE of 89.4% at  $P_{\text{abs}} = -19.7$  dBm, with a power dynamic range (PDR) — defined as the input power range over which PCE exceeds 40% — of 27.7 dB, which is 15 dB wider than that of the CCDD rectifier. The proposed LCS-R1 achieves a peak PCE of 69% and a PDR of 22.9 dB under the same criterion.

The performance of the rectifiers varies with different load conditions, as illustrated in Fig. 22. This evaluation tests the proposed rectifiers (LCS-R1 and LCSAB-R2) across a load range of 20 k $\Omega$  to 300 k $\Omega$ . The LCS-R1 rectifier achieves a peak PCE of 71.9% at a load resistance of 300 k $\Omega$ . The LCSAB-R2 rectifier demonstrates its best performance at 200 k $\Omega$ . The peak PCE of LCSAB-R2 shows minimal dependence on load variation, with only a 10.3% efficiency fluctuation across the tested load range. Although the PCE of LCS-R1 shows

greater variation across load resistances, it maintains a relatively high efficiency at higher load resistance values.

Fig. 23 shows the output voltage waveforms of the proposed rectifiers (LCS-R1 and LCSAB-R2) when  $V_{\text{out}} = 1$  V. The LCS-R1 reaches steady state faster than the LCSAB-R2, while the LCSAB-R2 exhibits a smaller voltage ripple. Fig. 24 shows the layout of the three circuits, designed using a TSMC 40 nm CMOS process.

To fairly quantify the trade-off between PCE and the operational input power range, we define a figure of merit (FoM) as:

$$\text{FoM} = \text{Peak PCE} \times \text{PDR} \quad (14)$$

where Peak PCE denotes the maximum power conversion efficiency (expressed in %), and PDR (power dynamic range) represents the input power span (in dB) over which the PCE exceeds 40%. As shown in Fig. 25, the proposed LCSAB-R2 rectifier achieves the highest FoM among all compared designs. To ensure a fair comparison, the DR and PCE data for all reference works are extracted directly from the original figures in their respective publications and re-evaluated using the same criterion of  $\text{PCE} > 40\%$ . Superimposed on the plot are iso-FoM contours ( $\text{FoM} = 5, 10, 15, 20, 25$ ), which clearly highlight the performance advantage of the proposed scheme.

Table 2 presents a summary and comparison of the proposed rectifiers against state-of-the-art CMOS rectifiers. To ensure a fair comparison, simulation results from the original studies are included in the table when available. The table includes several works focused on extending the dynamic range of CMOS rectifiers [14,20–23,25].

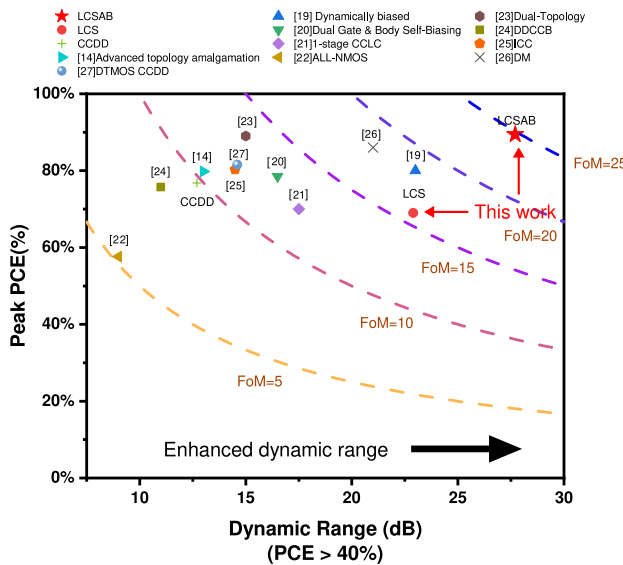


**Fig. 25.** Peak PCE vs dynamic range for state-of-the-art RF rectifiers, with iso-FoM contours.

This work is designed for operation at 433 MHz, which is a globally available frequency for RF energy harvesting applications, similar to 900 MHz [28]. Although the rectifier proposed in [23] achieves a peak PCE of 89%, its high efficiency is limited to low input power levels, whereas the LCSAB-R2 maintains a high PCE across the entire dynamic range. The proposed LCSAB-R2 achieves a higher peak PCE than those reported in other studies, while both LCS-R1 and LCSAB-R2 demonstrate improved PDR over existing designs.

#### 4. Conclusion

This article presents a leakage-current-suppression (LCS) technique to improve power conversion efficiency (PCE) by effectively mitigating reverse leakage current and power dissipation in rectifying transistors. The implementation methodology of the proposed technique is also discussed in detail. For validation, two rectifiers (designated as LCS-R1 and LCSAB-R2) were implemented using a TSMC 40 nm CMOS process. The LCSAB-R2 incorporates additional gate adaptive biasing and dynamic substrate biasing techniques to extend its input power dynamic range (PDR). Post-simulation results show that both proposed rectifiers achieve wide power dynamic ranges. Specifically, LCS-R1 and LCSAB-R2 achieve dynamic ranges of 22.9 dB and 27.7 dB, respectively, representing substantial improvements over conventional CCDD rectifiers.

#### CRediT authorship contribution statement

**Di Luo:** Writing – original draft, Methodology, Investigation, Formal analysis. **Jian Liu:** Writing – review & editing, Investigation, Funding acquisition. **Kang Zeng:** Writing – original draft, Validation. **Rui Wang:** Writing – original draft, Data curation. **Meijing Wang:** Writing – original draft, Investigation.

#### Declaration of competing interest

The authors declare that they have no known competing financial interests or personal relationships that could have appeared to influence the work reported in this paper.

#### Data availability

No data was used for the research described in the article.

#### References

- [1] Perera C, Liu CH, Jayawardena S, Chen M. A survey on internet of things from industrial market perspective. *IEEE Access* 2014;2:1660–79.
- [2] Kulkarni RD, Majid M, et al. Energy-efficient architecture for high-performance FIR adaptive filter using hybridizing CSDTCSE-CRABRA based distributed arithmetic design: Noise removal application in IoT-based WSN. *Integration* 2024;97:102172.
- [3] Elsayed O, Abouzied M, Vaidya V, Ravichandran K, Sánchez-Sinencio E. An ultralow-power RF wireless receiver with RF blocker energy recycling for IoT applications. *IEEE Trans Microw Theory Tech* 2018;66(11):4927–42.
- [4] Shafique K, Khawaja BA, Sabir F, Qazi S, Mustaqim M. Internet of things (IoT) for next-generation smart systems: A review of current challenges, future trends and prospects for emerging 5G-IoT scenarios. *IEEE Access* 2020;8:23022–40.
- [5] Hemour S, Wu K. Radio-frequency rectifier for electromagnetic energy harvesting: Development path and future outlook. *Proc IEEE* 2014;102(11):1667–91.
- [6] Chen D, Li R, Xu J, Li D, Fei C, Yang Y. Recent progress and development of radio frequency energy harvesting devices and circuits. *Nano Energy* 2023;108845.
- [7] Ramalingam L, Mariappan S, Parameswaran P, Rajendran J, Nitesh RS, Kumar N, Nathan A, Yarman BS. The advancement of radio frequency energy harvesters (RFEHs) as a revolutionary approach for solving energy crisis in wireless communication devices: A review. *IEEE Access* 2021;9:106107–39.
- [8] Almousouri AS, Ouda MH, Salama KN. A CMOS RF-to-DC power converter with 86% efficiency and 19.2-dBm sensitivity. *IEEE Trans Microw Theory Tech* 2018;66(5):2409–15.
- [9] Kotani K, Sasaki A, Ito T. High-efficiency differential-drive CMOS rectifier for UHF RFIDs. *IEEE J Solid-State Circuits* 2009;44(11):3011–8.
- [10] Ouda MH, Khalil W, Salama KN. Wide-range adaptive RF-to-DC power converter for UHF RFIDs. *IEEE Microw Wirel Components Lett* 2016;26(8):634–6.
- [11] Ouda MH, Khalil W, Salama KN. Self-biased differential rectifier with enhanced dynamic range for wireless powering. *IEEE Trans Circuits Syst II: Express Briefs* 2016;64(5):515–9.
- [12] Alhoshyany A. A 900 MHz, wide-input range, high-efficiency, differential CMOS rectifier for ambient wireless powering. *Sensors* 2022;22(3):974.
- [13] Chong G, Ramiah H, Yin J, Rajendran J, Mak P-I, Martins RP. A wide-PCE-dynamic-range CMOS cross-coupled differential-drive rectifier for ambient RF energy harvesting. *IEEE Trans Circuits Syst II: Express Briefs* 2019;68(6):1743–7.
- [14] Choo A, Lee YC, Ramiah H, Chen Y, Mak P-I, Martins RP. A high-PCE range-extension CMOS rectifier employing advanced topology amalgamation technique for ambient RF energy harvesting. *IEEE Trans Circuits Syst II: Express Briefs* 2023;70(10):3747–51.
- [15] Wong S-Y, Chen C. Power efficient multi-stage CMOS rectifier design for UHF RFID tags. *Integration* 2011;44(3):242–55.
- [16] Guler U, Ghovanloo M. Power management in wireless power-sipping devices: A survey. *IEEE Circuits Syst Mag* 2017;17(4):64–82.
- [17] Alhoshyany A. A CMOS adaptive 433/900 MHz differential RF power harvester with wide-dynamic range for wireless powering. *J Circuits Syst Comput* 2021;30(14):2150257.
- [18] Lu Y, Dai H, Huang M, Law M-K, Sin S-W, Seng-Pan U, Martins RP. A wide input range dual-path CMOS rectifier for RF energy harvesting. *IEEE Trans Circuits Syst II: Express Briefs* 2016;64(2):166–70.
- [19] Abdolrazzaghi M, Genov R, Eleftheriades GV. Time-multiplexed beam-steering antenna arrays for extended-coverage rf powering of multiple CMOS brain implants. *IEEE Microw Wirel Technol Lett* 2025.
- [20] Mohamed AR, Al-Khulaifi A, Al-Absi MA. An efficient CMOS RF-dc rectifier based on a dual dynamic self-biasing approach. *IEEE Access* 2025.
- [21] Chen Q, Huang M, Xia T, Yin J, Liu H, Martins RP, Lu Y. A radio-frequency cross-connected rectifier with LC source degeneration. *IEEE Trans Circuits Syst I Regul Pap* 2023;71(2):573–82.
- [22] Li X, Wang K, Zhou Y, Pan Y, Meng F, Ma K. A wide input range All-NMOS rectifier with gate voltage boosting technique for wireless power transfer. *IEEE Trans Circuits Syst II: Express Briefs* 2023;70(11):4023–7.
- [23] Choo A, Ramiah H, Churchill KKP, Chen Y, Mekhilef S, Mak P-I, Martins RP. A high-performance dual-topology CMOS rectifier with 19.5-db power dynamic range for RF-based hybrid energy harvesting. *IEEE Trans Very Large Scale Integr (VLSI) Syst* 2023;31(8):1253–7.
- [24] Moghaddam AK, Choo ACC, Ramiah H, Churchill KKP. A self-protected, high-efficiency CMOS rectifier using reverse dc feeding self-body-biasing technique for far-field RF energy harvesters. *AEU-Int J Electron Commun* 2022;152:154238.

- [25] Chong G, Ramiah H, Yin J, Rajendran J, Mak P-I, Martins RP. A wide-PCE-dynamic-range CMOS cross-coupled differential-drive rectifier for ambient RF energy harvesting. *IEEE Trans Circuits Syst II: Express Briefs* 2021;68:1743–7.
- [26] Almansouri AS, Kosek J, Salama KN. A dual-mode nested rectifier for ambient wireless powering in cmos technology. *IEEE Trans Microw Theory Tech* 2020;68(5):1754–62.
- [27] Asli ANF, Wong YC. - 31 dbm sensitivity high efficiency rectifier for energy scavenging. *AEU-Int J Electron Commun* 2018;91:44–54.
- [28] Yang G, Zhang K, Meratnia N, Havinga PJ. Finding optimum settings for a 433mhz radio for long range communication. In: 2015 2nd international conference on information science and control engineering. IEEE; 2015, p. 239–44.